Ba_2TeO: a new layered oxytelluride

T. Besara[a], D. Ramirez[a,b], J. Sun[a,b,c], J. B. Whalen[a,d], T. D. Tokumoto[a], S. A. McGill[a], D. J. Singh[c], T. Siegrist[a,b]

[a] National High Magnetic Field Laboratory, Condensed Matter Sciences Department, 1800 E. Paul Dirac Dr., Tallahassee, FL, 32310

[b] Florida Agricultural and Mechanical University-Florida State University College of Engineering, Department of Chemical and Biomedical Engineering, 2525 Pottsdamer St., Tallahassee, FL 32310

[c] Oak Ridge National Laboratory, 1 Bethel Valley Road, Oak Ridge, TN 37831

[d] Specialized Crystal Processing, Inc., 400 Capital Circle SE, Suite 18227, Tallahassee, FL, 32301

Abstract

Single crystals of the new semiconducting oxytelluride phase, Ba_2TeO, were synthesized from barium oxide powder and elemental tellurium in a molten barium metal flux. Ba_2TeO crystallizes in tetragonal symmetry with space group *P*4/*nmm* (#129), a = 5.0337(1) Å, c = 9.9437(4) Å, Z = 2. The crystals were characterized by single crystal x-ray diffraction, heat capacity and optical measurements. The optical measurements along with electronic band structure calculations indicate semiconductor behavior with a band gap of 2.93 eV. Resistivity measurements show that Ba_2TeO is highly insulating.

1. Introduction

Oxychalcogenides make up an active field of research, as these materials show promise in a variety of fields, such as, e.g., optoelectronics [1, 2], superconductors (see, for instance the review by Johnston [3] and references therein) , and more recently, as thermoelectrics [4-7]. Another area in which oxychalcogenides have been extensively investigated is their use as transparent conductors and semiconductors [8-11], with the layered copper-based oxychalcogenides standing out [12-22]. Many of the interesting properties of the oxychalcogenides stem from their parent oxide and

chalcogenide phases, with structural motifs still present as modified arrangements in the resulting oxychalcogenides.

Among semiconducting oxychalcogenides, oxysulfides and oxyselenides have been extensively investigated, in contrast to the oxytellurides. Tellurates and tellurites, tellurium-based compounds containing cationic $Te^{4+/6+}$ present as TeO_4^{2-} or TeO_4^{4-} anions, have been studied extensively [23-25], as well as semiconducting tellurides (compounds with anionic Te^{2-}) [26-28]. Oxytellurides, on the other hand, are rarer, with uranium oxytellurides UOTe [29, 30], U_2O_2Te [31], and $U_4O_4Te_3$ [30, 32, 33] studied in more details. Furthermore, the physical properties of a number of the lanthanide oxytellurides Ln_2O_2Te have also been investigated [34, 35]. More recently, a new layered oxytelluride, $Ba_3Yb_2O_5Te$, has been discovered [36].

The complex orbital hybridizations in anion-ordered multinary crystals such as oxytellurides can give rise to properties that differ vastly from the respective tellurides and oxides. Here, we report on the synthesis and property measurements of a new layered oxytelluride, Ba_2TeO, comprised of alternating puckered BaTe and BaO layers. Optical property measurements and theoretical calculations show Ba_2TeO to be a semiconductor with a band gap of 2.93 eV.

2. Experimental and computational methodology

The Ba_2TeO crystals were prepared from a barium metal flux, with 1 mmol of BaO and elemental Te for every 20mmol of Ba metal. The starting materials are sealed in a stainless steel crucible using an arc welder under inert (argon) atmosphere in a glovebox. The steel crucibles are subsequently sealed in quartz tubing under vacuum. The sample were heated in 10 hours to 1000 °C, solvated for 20 hours, and cooled over 50 hours to 820 °C, followed by centrifugation to separate the flux from crystals that formed. Large single crystal platelets with dimensions up to several millimeters were obtained in this way. The Ba_2TeO crystals had a metallic lustre with dark greyish to black appearance and were relatively brittle and tended to exfoliate and cleave easily. Crystals decomposed in the ambient at a moderate rate. To maintain sample integrity, all crystals used for subsequent analysis were handled and stored under inert atmosphere at all times possible.

Elemental analysis using EDS in a JEOL 5900 scanning electron microscope confirmed the stoichiometry of Ba_2TeO having a molar Ba:Te ratio of 2:1 across varying locations on multiple single crystals to within 5 at.% deviation.

The Ba_2TeO crystals were structurally characterized by single crystal x-ray diffraction (XRD) with an Oxford-Diffraction Xcalibur2 CCD system using graphite-monochromated MoKα radiation. Samples were suspended in Paratone-N oil in a cryoloop, and cooled with an Oxford-Diffraction Cryojet to a temperature of 200 K. Reflections were recorded, indexed and corrected for absorption using the Oxford-Diffraction CrysAlisPro software [37], and subsequent structure determination and refinement was carried out using CRYSTALS [38]. A CIF has been deposited with the FIZ-Karlsruhe (ICSD #428396) [39].

A Quantum Design PPMS system was used to measure the zero-field heat capacity between 2 K and room temperature, with crystals embedded in grease. Electrical resistivity was measured using 4-point contacts on samples of various thickness, but all samples studied were found to be highly resistive.

Optical absorption spectroscopy was performed on single crystal samples. Thin layers of Ba_2TeO crystals were obtained by exfoliating large single crystals with adhesive tape. The process was repeated until the samples became visibly transparent. The thin layer was then mounted on a copper pinhole 600 μm in diameter using the adhesive tape as substrate; a reference pinhole of 600 μm was prepared using the same adhesive tape. The sample and reference were mounted in a cylinder that was sealed with fused silica windows on either end, and purged under a constant flow of nitrogen to protect the sample from oxidation. The spectrum was measured using an Ocean Optics LS-1 light source and USB2000 spectrometer in the wavelength range from 450 to 1000 nm. For UV-VIS absorption between 300 and 500 nm, a deuterium light source coupled with an Acton SP2300 spectrometer and back-illuminated, liquid nitrogen cooled CCD were used.

First-principle calculations of the electronic structure and optical properties, based on density functional theory (DFT) [40, 41], were carried out using the WIEN2k code [42], which employs the full-potential linearized augmented plane-wave and local orbitals (FP-LAPW+lo) method [43]. In order to obtain a more accurate band gap, the modified Becke-Johnson (mBJ) method [44] was used for the exchange-correlation potential. The LAPW sphere radii employed were 2.6 Bohr for both barium and tellurium, and 2.0 Bohr for oxygen. The cut-off parameter for the plane wave basis was $R_{min}K_{max}=7$, where $R_{min}=2$ Bohr is the smallest sphere radius. The convergence was tested and an 8×8×8 k-mesh for band structure calculations and a 16×16×16 k-mesh for optical properties calculations was employed. Because of the relatively heavy elements barium and tellurium, spin-orbit coupling was also included.

3. Results and Discussion

The growth of single crystalline Ba_2TeO so far is possible in the molten metal flux only, as presented in this report and elsewhere [45]. Direct solid state reactions produce only the binary compounds BaTe and BaO, but not Ba_2TeO, likely due to incongruent melting of the phase. The Ba metal flux, in this case, allows simultaneous solubility of oxygen as well as Te and allows the formation of Ba_2TeO at moderate temperatures.

3.1 Structure and Strain

The Ba_2TeO single crystal grew in a structure with tetragonal symmetry and space group *P*4/*nmm* (#129). Results of the XRD refinement are summarized in Table 1, along with selected interatomic distances and angles.

Table 1

Single crystal x-ray diffraction data and collection parameters (collected at 200 K), atom positions, and selected distances and angles.

Formula	**Ba_2TeO**
Formula weight	418.26 g/mol
Space group	*P4/nmm* (#129) origin 2
Cell parameters	a = 5.0337(1) Å, c = 9.9437(4) Å
Volume	251.96(2) Å^3
Z	2
$D_{calc.}$	5.513 g/cm^3
μ	21.029 mm^{-1}
Data collection range	4.099° < θ < 66.506°
Reflections collected/independent	11169/1359
Parameters refined	13
R_1, wR_2	0.0751[a], 0.0769[b]
Goodness-of-fit	1.2831

Refined atomic positions							Ideal atomic positions			
Atom	**Site**	**Occ.**	**x**	**y**	**z**	**U_{eq}**	**Atom**	**x**	**y**	**z**
Ba1	2c	1	3/4	3/4	0.16449(6)	0.0110(2)	Ba1	3/4	3/4	1/6
Ba2	2b	1	1/4	3/4	1/2	0.0109(2)	Ba2	1/4	3/4	1/2
Te	2c	1	1/4	1/4	0.20113(7)	0.0115(2)	Te	1/4	1/4	1/6
O	2c	1	3/4	3/4	0.4110(8)	0.0118(2)	O	3/4	3/4	1/2

Selected distances (Å)	
Ba1 – O	2.451(1)
Ba2 – O	2.668(1)
Ba1 – Te, along [110]	3.578(1)
Ba1 – Te, along [001]	3.636(1)
Te – O	3.857(1)

Selected angles (°)	
Ba1 – Te – Ba1, along [110]	168.31(3)
Ba2 – O – Ba2, along [100] or [010]	141.25(1)
Te – Ba1 – O, along [001]	180.00

[a] $R_1 = \Sigma \| F_o | - | F_c \| / \Sigma | F_o \|$.

[b] $wR_2 = [\Sigma\, w(F_o^2 - F_c^2)^2 / \Sigma\, w(F_o^2)^2]^{1/2}$, $w = [\sigma^2(F_o^2) + (A \cdot p)^2 + B \cdot p]^{-1}$; $p = (F_o^2 + 2F_c^2)/3$; A = 0.0067, B = 0.

The structure of Ba_2TeO is literally a combination of alternating layers of BaTe (containing Ba1) and BaO (containing Ba2), stacked in the *c* direction. The *parent* BaTe and BaO phases both crystallize in the NaCl (rocksalt) structure type. While BaTe possesses a high pressure phase with the CsCl structure type, a high pressure phase of BaO (HP-BaO) exists that is closely related to the PbO-type structure and also crystallizes in the space group symmetry *P4/nmm* (#129) [25]. The very differing bonding distances present in BaO and BaTe are accommodated in Ba_2TeO by a two-dimensional layering of its structure, and the ratio of the two bond distances Ba–O and Ba–Te needs to be within an acceptable range in regard to lattice mismatch. A simple stacking arrangement that accommodates layers with different internal bond distances is a tetragonal unit cell, where the long bonds (Ba–Te) are aligned with the [110] direction and the short bonds (Ba–O) along the [100] direction. For this arrangement, the ratio between the two bond distances should be

$$\frac{d(\mathrm{Ba-O})}{d(\mathrm{Ba-Te})} = \frac{1}{\sqrt{2}}.$$

For a simple arrangement of one BaTe layer and one BaO layer, there can be two different types of contacts along the *c*-axis: either $[Ba–Ba]_n$ contacts, or $[Ba–Te]_n$ contacts. If two BaTe layers alternate with one BaO layer, $[BaTe–BaTe–Ba_2O_2]_n$ stacking forms along the *c*-axis. Furthermore, if the bond distance ratio differs from this ideal ratio, deviations from the ideal structure are expected, optimizing the bonding between the atoms.

Using space group *P*4/*nmm* (#129) and an ideal ratio *c*/*a*=2, ideal atom positions can be obtained and are listed in Table 1. In this ideal structure, three layers, two BaTe layers and one Ba_2O_2 layer, alternate along the *c*-axis, with the layers at *z*=1/6, 1/2, and 5/6. Note that the symmetry of this ideal structure is *P*4/*mmm*, while the actual space group of Ba_2TeO, *P*4/*nmm*, allows for distortions to be accommodated. Using a unit cell parameter of a = 5 Å, the in-plane Ba–Te distance in the ideal structure is $5/\sqrt{2} \approx 3.54$ Å, in agreement with the distance of approximately 3.5 Å found in rocksalt type BaTe [25]. For the ideal, flat BaO layer, the Ba–O distance in this arrangement is then 2.5 Å, whereas rocksalt type BaO shows a distance of approximately 2.75 Å [25], a 9% mismatch. In this arrangement, the Ba–Te bond dominates the structure, and the Ba–O bond is in strong compression, with structural relaxation expected, where either the oxygen atom or the barium atom moves out of the plane parallel to the *c*-axis towards a BaTe layer. With distances between the layers of *c*/3 (about 3.33 Å) indicating weak bonding, the oxygen atom moving towards the BaTe layer will induce stronger bonding between the layers.

For the Ba1–O and the Ba2–O distances to become equal under the condition that only the oxygen atoms move parallel to the *c*-axis and the barium atoms remain in the original plane, the oxygen displacement in fractional coordinates is

$$z = \left(\frac{1}{4} \frac{a^2}{c^2} - \frac{1}{9} \right) \frac{2}{3} = -0.0729,$$

resulting in a Ba1–O = Ba2–O distance of 2.6 Å, within 5.5% of the expected distance for Ba–O in rocksalt BaO. Displacement in the opposite direction results in longer Te–O contacts; therefore half of the oxygen atoms move up towards Ba1 in the BaTe rocksalt-like layer above, while the other half move down towards the Ba1 in the BaTe rocksalt-like layer below, producing a puckered BaO layer. This BaO layer is closely related to the corresponding layer in HP-BaO, where moving the Ba atoms out of the BaO planes, with the oxygen atoms remaining in the original plane, accommodates the external strain. In the case of Ba_2TeO, the accommodation of the in-plane strain, however, produces *inverse* PbO-type layers, since the oxygen atoms move, while the barium atoms remain in the ideal layer. Finally, the BaTe layer slightly puckers so that the fully relaxed structure connects the BaTe layers with the BaO layers via a short Ba–O bond. Thus, the fully relaxed structure of Ba_2TeO resembles that of ZrSiCuAs (filled PbFCl structure-type) [46], with inverse PbO-type BaO layers separated by slightly distorted NaCl-type BaTe layers. The *c*/*a* ratio of the fully relaxed structure is approximately 1.976, very close to the ideal ratio of 2. The short *inter*layer

Ba1–O bond is 2.451 Å, while the *intra*layer Ba2–O bond is 2.668 Å, within 3% of the Ba–O distance in rocksalt-type BaO. The displacement of oxygen out of plane is clearly manifest in the Ba2–O–Ba2 angle of 141° (as compared to the ideal rocksalt angle of 180°), while the puckering of the BaTe layer results in a Ba1–Te–Ba1 angle of 168° (selected distances and angles are listed in Table 1). The displacements in the structure of Ba_2TeO are illustrated in Figure 1, showing first the ideal structure (Figure 1a) with NaCl-type layers only, followed by the structure where the oxygen atoms are moved parallel to the c-axis, creating the inverse PbO-type layer (Figure 1b), and finally the actual structure with the additional puckering of the BaTe layers (Figure 1c).

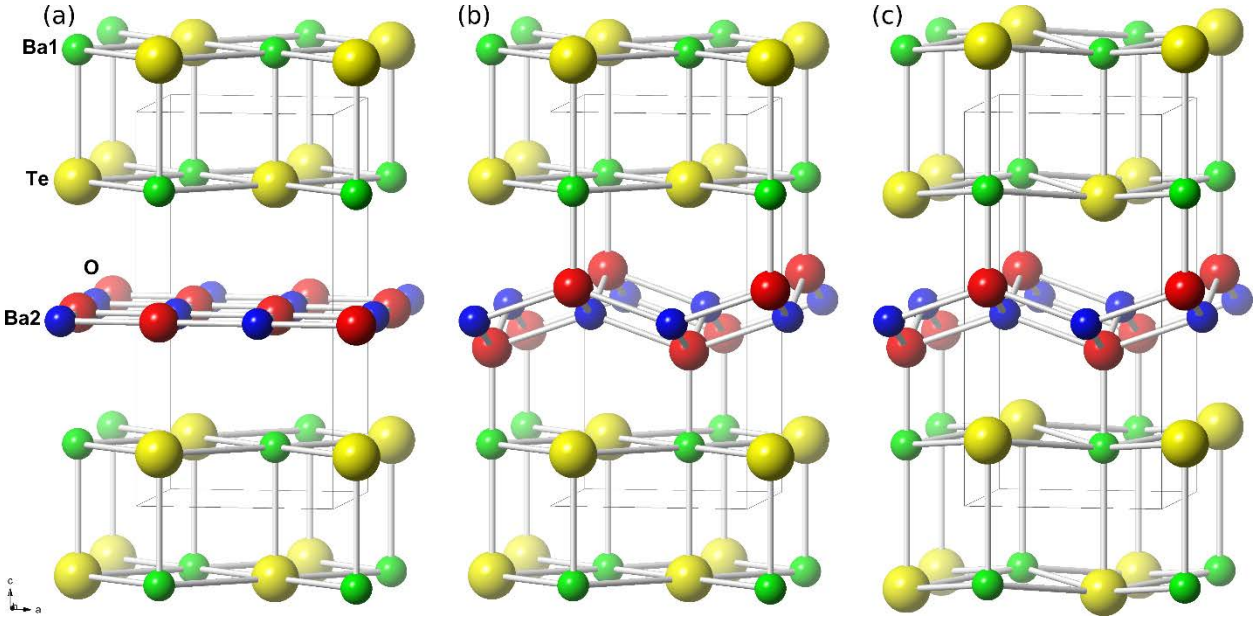

Figure 1: (a) Ideal structure of layered BaO and BaTe, (b) structure where the oxygen atoms are displaced, and finally (c) the actual structure of Ba_2TeO with puckered BaTe layers.

The bond valence sum (BVS) of Ba1 is 1.90, indicating underbonding of the barium in the BaTe layer, despite the short interlayer Ba1–O bond. The Ba2 in the BaO layer is similarly underbonded as indicated by its BVS of approximately 1.86, and is most likely due to the lack of apical atoms in the Ba2 coordination.

The stability of other possible 2-1-1 alkaline earth oxychalcogenide phases can now be discussed in view of a stability factor based on their respective rocksalt bond distances. For the case of Ba_2SO and Ba_2SeO, for example, the shorter Ba–S/Se distance would put an additional

compression on the Ba–O distances, and therefore, with the exception of Ba_2TeO, no other barium oxychalcogenide phase exists in this system. Replacing barium with the smaller alkaline earth metals (Sr, Ca, and Mg), may produce potential candidates for isostructural phases. A simple tolerance stability factor based on the respective rocksalt distances (SF_{NaCl}) can now be defined as

$$SF_{NaCl} = \frac{d(AE - O)}{d(AE - X)} \times \sqrt{2},$$

where AE = Mg, Ca, Sr, and Ba, and X = S, Se, and Te. For Ba_2TeO, using this method, SF_{NaCl}=1.118 if the respective distances from the corresponding rocksalt phases BaO and BaTe are used. Using the distances from the actual structure yields a stability factor of 1.055. Values for the tolerance factor for various combinations of AE_2XO using the respective rocksalt distances are listed in Table 2. A continued search for a synthesis route to grow single crystals of Ba_2TeO analogs from alkaline-earth and chalcogenide substitutions is ongoing.

Table 2

Tolerance (stability) factor for various phases using rocksalt distances.

Composition	**SF_{NaCl} (rocksalt)**
Mg_2SO	1.147
Mg_2SeO	1.089
Mg_2TeO	1.009
Ca_2SO	1.195
Ca_2SeO	1.146
Ca_2TeO	1.072
Sr_2SO	1.212
Sr_2SeO	1.170
Sr_2TeO	1.095
Ba_2SO	1.218
Ba_2SeO	1.178
Ba_2TeO	1.118

3.2 Density of states

The density of states plot in Figure 2 show a band gap of approximately 2.5 eV, indicating that Ba_2TeO is a semiconductor. The valence states in the region -2.2 – 0 eV are mainly occupied by the Te 5*p* and O 2*p* states, with the Te 5*p* dominating the valence band edge near zero. The relatively narrow valence band width is an indication of weak interactions between the Te anions, which may cause heavy electron effective masses. A small overlap between Te 5*p*/O 2*p* orbitals

and Ba 5*d* orbitals in the region between -2 and 0 eV indicates hybridization between these orbitals, generating a weak covalency. Nominally, Ba^{2+} has unoccupied 5*d* orbitals, while Te^{2-} has fully occupied 5*p* orbitals. In this compound there is a clear mixing of Ba 5*d* states in the occupied states, indicative of this covalency. The conduction bands in the region 2.5–12 eV are dominated by the two inequivalent Ba 5*d* states with small amounts of Te 5*p* and O 2*p* anti-bonding states. Furthermore, the Te $5s^2$ orbitals (not shown here) are quite localized from -9.2 to -8.5 eV, with little Ba 5*p* orbitals overlap. However, the charge density map does not show an asymmetric character of the overall Te $5s^2$ lone pair and indicates little to no stereochemical activity [47]. This is as expected since in this compound Te is anionic, with a nominally full 5*p* shell and cation, rather than anion, neighbors.

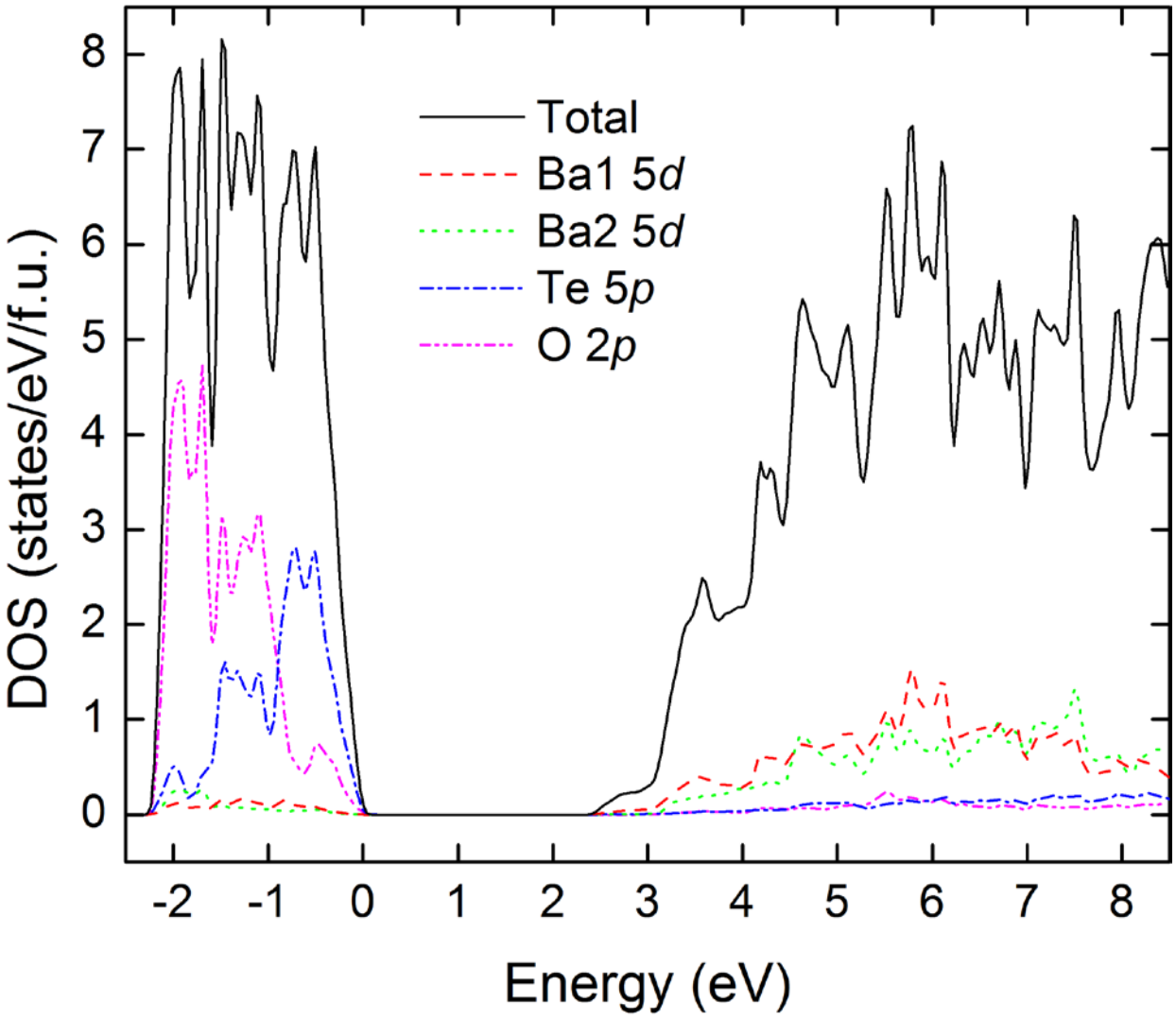

Figure 2: Total and partial density of states.

3.3 Heat Capacity

The temperature dependence of heat capacity for a 4 mg sample of Ba_2TeO is shown in Figure 3. The small inset (a) illustrates the low-temperature region, plotted as C_P/T vs T^2. This low temperature behavior is described by

$$\frac{C_P}{T} = \beta T^2,$$

since the electronic contribution to the heat capacity is zero, consistent with semiconducting Ba_2TeO. The low temperature data yields the lattice contribution $\beta \approx 2.0 \pm 0.3$ mJ/mol·K^4, and the Debye temperature θ_D can be estimated via the relation [48, 49]

$$\theta_D = \sqrt[3]{\frac{12\pi^4 Rn}{5\beta}}.$$

Here, n denotes the number of atoms per formula unit (n=4 for Ba_2TeO) and R the molar gas constant, yielding a Debye temperature of $\theta_D \approx 158 \pm 8$ K.

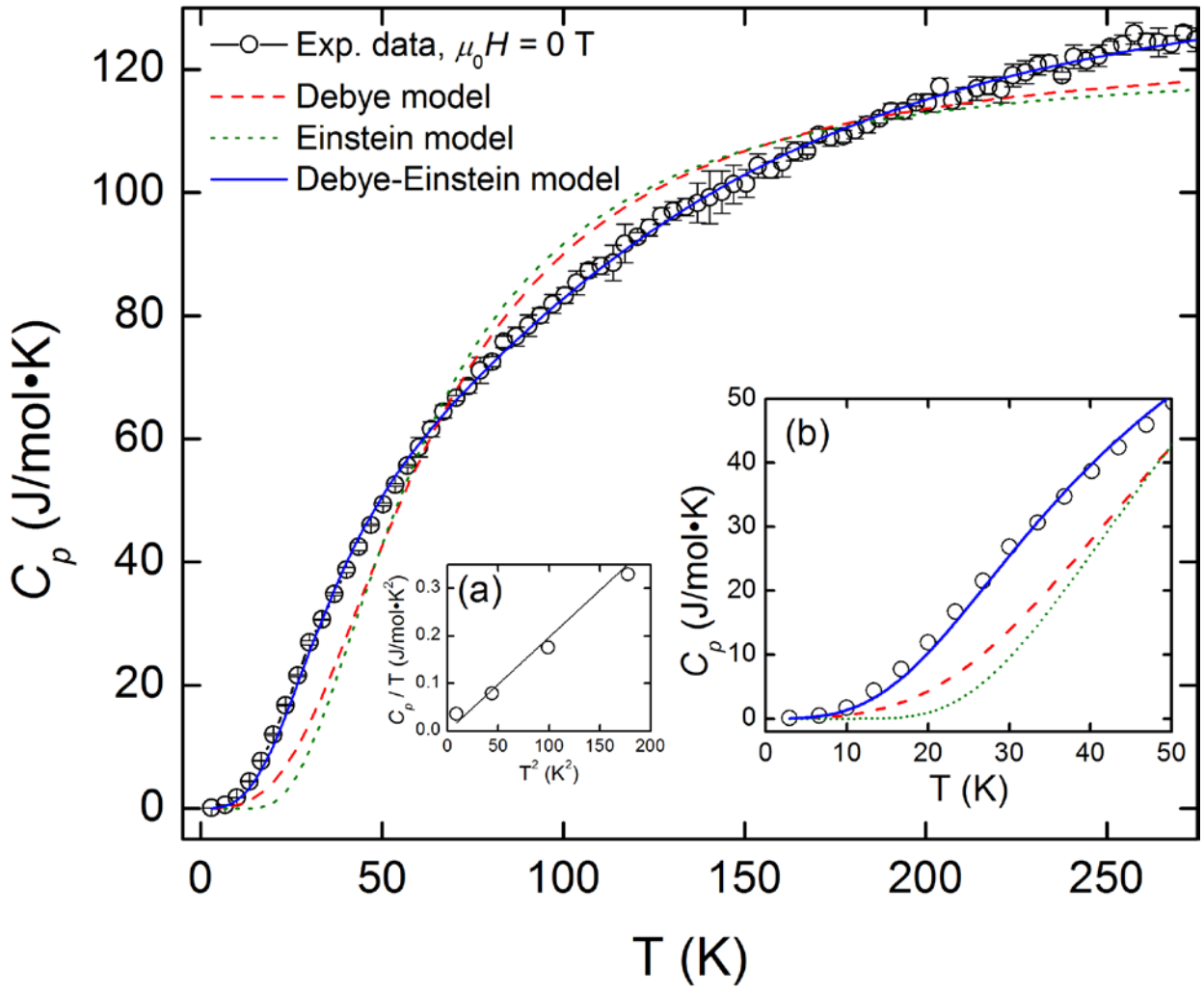

Figure 3: Temperature dependence of the heat capacity of Ba_2TeO, obtained at zero applied field. The solid blue line is a fit to a combined Debye-Einstein model, while the dashed red and dotted green are fits to the separate Debye and Einstein models, respectively. Inset (a) displays the low temperature linearity of C_P/T vs T^2. Inset (b) is a close-up of the low temperature region with the three different models.

To gain further insight in the lattice dynamics, the full temperature range of the measured heat capacity is considered. A Debye or single Einstein mode model cannot adequately describe the temperature dependence of the heat capacity, as is clearly seen in the fit of the data to the two models (Figure 3 and inset (b) for the low temperature region). A combined model, on the other hand, including the contribution of a Debye and an Einstein model, describes the heat capacity adequately: $C_P = C_D + C_E$ with

$$C_P = c_D\left(\frac{T}{\theta_D}\right)^3 \int_0^{\theta_D/T} \frac{x^4 e^x}{\left(e^x - 1\right)^2} dx + c_E\left(\frac{\theta_E}{T}\right)^2 \frac{e^{\theta_E/T}}{\left(e^{\theta_E/T} - 1\right)^2},$$

where $x = \hbar\omega/k_B T$, ω is the Debye frequency, θ_D and θ_E are the Debye and Einstein temperatures, respectively, and c_D and c_E are constants containing numbers of oscillators and degrees of freedom. These four parameters are treated as fitting parameters, and the combined model adequately describes the experimental data over the entire temperature range (solid line in Figure 3). The Debye and Einstein temperatures obtained are $\theta_D \approx 167 \pm 3$ K and $\theta_E \approx 486 \pm 11$ K, respectively, with corresponding constants $c_D \approx 248 \pm 4$ J/mol·K and $c_E \approx 56 \pm 1$ J/mol·K. The Debye temperature is in good agreement with the value derived from the low temperature data. The two distinct temperatures, θ_D and θ_E, indicate the existence of two different vibrational modes in Ba_2TeO, consistent with the observation of two distinct structural moieties, BaTe and BaO. Since the BaO layer is under compression, it is expected to be stiff, thereby contributing to the heat capacity at higher temperatures, consistent with the higher Einstein temperature ascribed to this layer. The lower Debye temperature then corresponds to the BaTe layers and is consistent with the Debye temperature obtained from the low temperature data only.

3.5 Optical Absorbance

The absorbance spectrum spanning from the UV to NIR is displayed in Figure 4, for a single crystal where the electric field of the incident light was oriented in the plane of the sample, i.e., $E \perp c$-axis. As the UV range is approached, a sharp onset in absorbance is observed, which is a clear manifestation of a band edge. A linear extrapolation of the absorbance near the band edge intercepts the *x*-axis at 2.93 eV, which is assigned as the band gap energy.

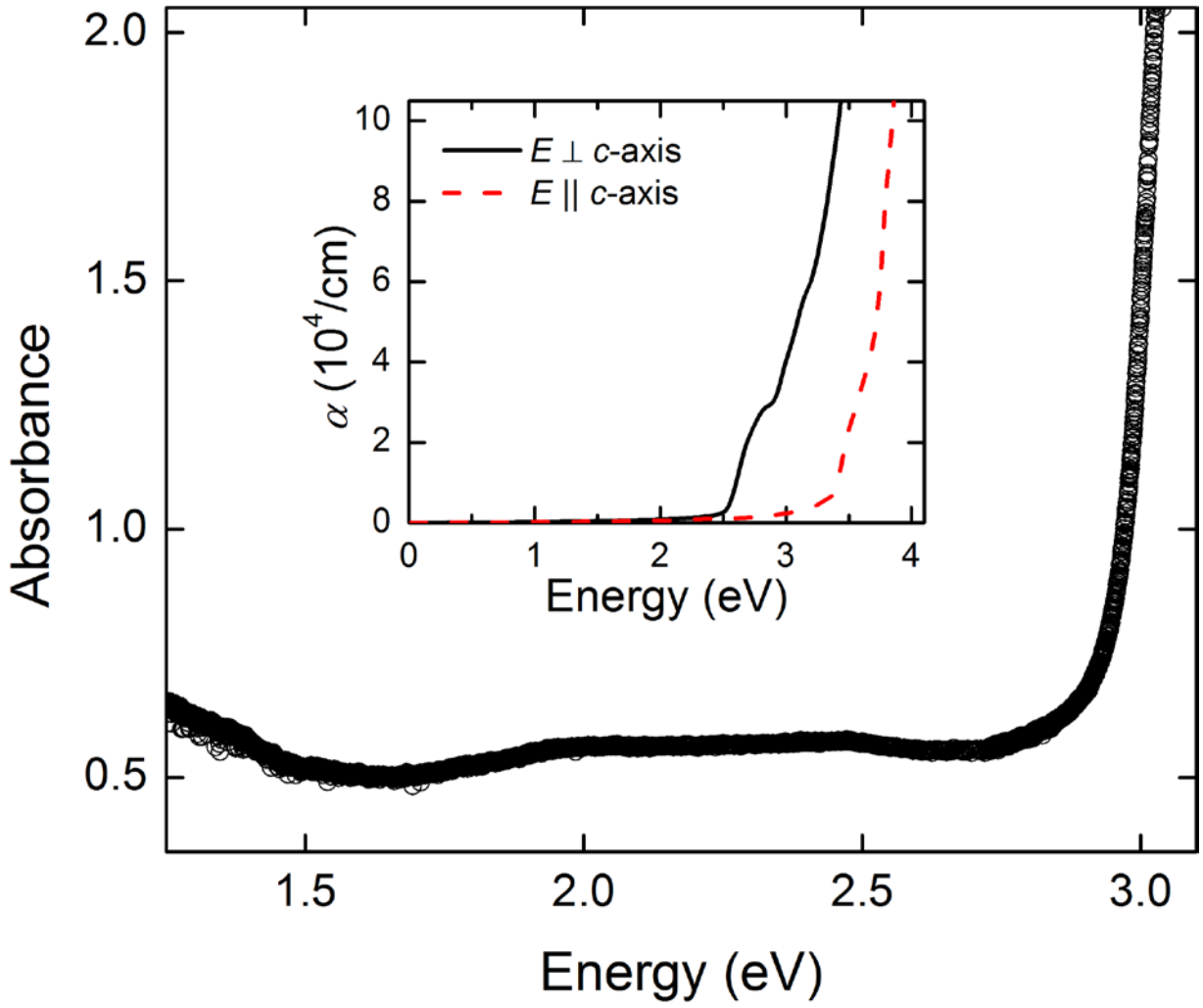

Figure 4: Absorbance as a function of energy from UV-VIS optical measurements. The electric field of the incident light was oriented in the plane of the sample ($E \perp c$-axis). The band gap energy is 2.93 eV, obtained by linear extrapolation of the absorbance near the band edge to the x-axis. The inset shows the calculated absorption coefficient as a function of energy for the electric field in two directions: perpendicular and parallel to the c-axis.

By calculating the dielectric tensor, the optical properties for a material can be obtained. The total dielectric function $\varepsilon(\omega)$ is expressed as the sum of a real and an imaginary part, $\varepsilon(\omega)=\varepsilon_1(\omega)+i\varepsilon_2(\omega)$, with the absorption coefficient α calculated using the relation

$$\alpha = \frac{4\pi\kappa}{\lambda},$$

where κ is the extinction coefficient, obtained from $\varepsilon_1(\omega)$ and $\varepsilon_2(\omega)$ [50]. Since Ba_2TeO crystallizes with tetragonal symmetry, it has only two nonzero second order dielectric tensor components, $\varepsilon^{xx}(\omega)=\varepsilon^{yy}(\omega)$ and $\varepsilon^{zz}(\omega)$. Therefore, calculations were performed for both an electric field perpendicular and parallel to the *c*-axis. As can be seen in the inset to Figure 4, the absorption coefficient is anisotropic. The calculated absorption edge is approximately 2.5 eV in both orientations; however, the band gap energy differs clearly between the two orientations. In the case of an electric field perpendicular to the *c*-axis, a linear extrapolation of α intercepts the *x*-axis at approximately 2.9 eV, in good agreement with the experimental absorbance measurements. In the case of an electric field parallel to the *c*-axis, a linear extrapolation yields a band gap energy of approximately 3.6 eV, i.e., a nearly 25 % increase of the gap energy when compared to the $E \perp c$-axis case.

As grown crystals are not transparent, and thicker samples show optical absorption starting in the infrared region, extending to about 2.2eV. This absorption is likely due to midgap states due to impurities likely from the crucible. By exfoliating the samples, this defect absorption could be reduced, and thin samples were transparent to the eye.

4. Conclusion

A new layered oxytelluride, Ba_2TeO, has been synthesized in single crystalline form using a barium metal flux. Ba_2TeO is comprised of alternating inverse PbO-type BaO layers and slightly puckered NaCl-type BaTe layers in a ZrSiCuAs (filled PbFCl) structure type. The structure has tetragonal symmetry with space group *P*4/*nmm*, and has an almost ideal *c*/*a* ratio of 2. In this arrangement, the two types of layers containing structural rocksalt moieties can be combined if the tolerance factor is within a certain range: it is expected that other phases will form if the tolerance factor is about 1.00 to 1.12. Heat capacity data show that the relaxed BaTe dominates the heat capacity at lower temperatures, with the compressed, stiff, BaO layer contributing to the heat capacity at high temperatures. Optical absorbance measurements revealed a band gap of 2.93 eV, a value that is corroborated by calculations of the absorption coefficient and density of states.

Acknowledgements

This work is supported by the U.S. Department of Energy, Basic Energy Science, Materials Sciences and Engineering Division, under award DE-SC0008832. J.B.W. acknowledges support

by the State of Florida, Florida State University, and the Leon County Research and Development Authority. Work at the Oak Ridge National Laboratory was supported by the Department of Energy, Basic Energy Science, Materials Sciences and Engineering Division. J.S. acknowledges a graduate student fellowship, funded by the Department of Energy, Basic Energy Science, Materials Sciences and Engineering Division, through the ORNL GO! program. A portion of this work was performed at the National High Magnetic Field Laboratory, which is supported by the National Science Foundation Cooperative Agreement # DMR-1157490, the State of Florida, and the U.S. Department of Energy.

References

[1] H. Hiramatsu, H. Kamioka, K. Ueda, H. Ohta, T. Kamiya, M. Hirano, H. Hosono, *Physica Status Solidi (a)* 203 (2006) 2800-2811.
[2] H. Hiramatsu, H. Yanagi, T. Kamiya, K. Ueda, M. Hirano, H. Hosono, *Chemistry of Materials* 20 (2008) 326-334.
[3] D.C. Johnston, *Advances in Physics* 59 (2010) 803-1061.
[4] C. Barreteau, L. Pan, E. Amzallag, L.D. Zhao, D. Bérardan, N. Dragoe, *Semiconductor Science and Technology* 29 (2014) 064001(10).
[5] P. Vaqueiro, G. Guélou, M. Stec, E. Guilmeau, A.V. Powell, *Journal of Materials Chemistry A* 1 (2013) 520-523.
[6] D. Zou, S. Xie, Y. Liu, J. Lin, J. Li, *Journal of Materials Chemistry A* 1 (2013) 8888-8896.
[7] C. Barreteau, L. Pan, Y.-L. Pei, L.D. Zhao, D. Bérardan, N. Dragoe, *Functional Materials Letters* 6 (2013) 1370007(5).
[8] H. Ohta, K. Nomura, H. Hiramatsu, K. Ueda, T. Kamiya, M. Hirano, H. Hosono, *Solid-State Electronics* 47 (2003) 2261-2267.
[9] H. Hosono, *Thin Solid Films* 515 (2007) 6000-6014.
[10] T. Kamiya, H. Hosono, *International Journal of Applied Ceramic Technology* 2 (2005) 285-294.
[11] G.Q. Lin, H. Gong, P. Wu, *Physical Review B* 71 (2005) 085203(5).
[12] K. Ueda, S. Inoue, S. Hirose, H. Kawazoe, H. Hosono, *Applied Physics Letters* 77 (2000) 2701-2703.
[13] T. Kamiya, K. Ueda, H. Hiramatsu, H. Kamioka, H. Ohta, M. Hirano, H. Hosono, *Thin Solid Films* 486 (2005) 98-103.
[14] K. Ueda, H. Hiramatsu, M. Hirano, T. Kamiya, H. Hosono, *Thin Solid Films* 496 (2006) 8-15.
[15] S. Ramasubramanian, M. Rajagopalan, J. Kumar, R. Thangavel, *Journal of Applied Physics* 106 (2009) 023720(6).
[16] A.P. Richard, J.A. Russell, A. Zakutayev, L.N. Zakharov, D.A. Keszler, J. Tate, *Journal of Solid State Chemistry* 187 (2012) 15-19.
[17] Y. Ohki, K. Takase, Y. Takahashi, Y. Takano, K. Sekisawa, *Journal of Alloys and Compounds* 408-412 (2006) 98-100.

[18] M.L. Liu, L.B. Wu, F.Q. Huang, L.D. Chen, J.A. Ibers, *Journal of Solid State Chemistry* 180 (2007) 62-69.
[19] S.J. Clarke, P. Adamson, S.J.C. Herkelrath, O.J. Rutt, D.R. Parker, M.J. Pitcher, C.F. Smura, *Inorganic Chemistry* 47 (2008) 8473-8486.
[20] H. Kamioka, H. Hiramatsu, M. Hirano, K. Ueda, T. Kamiya, H. Hosono, *Journal of Luminescence* 112 (2005) 66-70.
[21] K. Ueda, H. Hosono, *Journal of Applied Physics* 91 (2002) 4768-4770.
[22] H. Hiramatsu, K. Ueda, H. Ohta, M. Hirano, T. Kamiya, H. Hosono, *Applied Physics Letters* 82 (2003) 1048-1050.
[23] G.W. Leddicotte, *The Radiochemistry of Tellurium*. Subcommittee on Radiochemistry, National Academy of Sciences-National Research Council, 1961.
[24] N.N. Greenwood, A. Earnshaw, *Chemistry of the Elements*. 2nd ed.; Butterworth-Heinemann, Oxford, UK, 1997.
[25] P. Villars, K. Cenzual, Pearson's Crystal Data - Crystal Structure Database for Inorganic Compounds. ASM International, Materials Park, Ohio, USA, 2012/13.
[26] B. Gil, D.J. Dunstan, *Semiconductor Science and Technology* 6 (1991) 428-438.
[27] A.M. Smith, S. Nie, *Accounts of Chemical Research* 43 (2010) 190-200.
[28] R.E. Bailey, S. Nie, *Journal of the American Chemical Society* 125 (2003) 7100-7106.
[29] A.J.K. Haneveld, F. Jellinek, *Journal of Inorganic & Nuclear Chemistry* 26 (1964) 1127-1128.
[30] L. Shlyk, J. Stępień-Damm, R. Troć, *Journal of Crystal Growth* 154 (1995) 418-421.
[31] E.W. Breeze, N.H. Brett, *Journal of Nuclear Materials* 40 (1971) 113-115.
[32] H. Noël, M. Potel, L. Shlyk, D. Kaczorowski, R. Troć, *Journal of Alloys and Compounds* 217 (1995) 94-96.
[33] D. Kaczorowski, R. Troć, L. Shlyk, H. Noël, A. Zaleski, *Journal of Magnetism and Magnetic Materials* 140-144 (1995) 1437-1438.
[34] F.A. Weber, T. Schleid, *Zeitschrift für Anorganische und Allgemeine Chemie* 625 (1999) 1833-1838.
[35] J. Llanos, S. Conejeros, R. Cortés, V. Sánchez, P. Barahona, O. Peña, *Materials Research Bulletin* 43 (2008) 312-319.
[36] J.B. Whalen, T. Besara, R. Vasquez, E. Herrera, J. Sun, D. Ramirez, R.L. Stillwell, S.W. Tozer, T.D. Tokumoto, S.A. McGill, J. Allen, M. Davidson, T. Siegrist, *Journal of Solid State Chemistry* 203 (2013) 204-211.
[37] Agilent Technologies, CrysAlisPro, Version 1.171.36.28. Agilent Technologies UK Ltd., Oxford, UK, 2012.
[38] P.W. Betteridge, J.R. Carruthers, R.I. Cooper, K. Prout, D.J. Watkin, *Journal of Applied Crystallography* 36 (2003) 1487. CRYSTALS version 14.40b was used for the refinement.
[39] G. Bergerhoff, I.D. Brown, in: F.H. Allen, G. Bergerhoff, R. Sievers, (Eds.), Crystallographic Databases, International Union of Crystallography, Chester, 1987, pp. 77-95.
[40] P. Hohenberg, W. Kohn, *Physical Review* 136 (1964) B864-B871.
[41] W. Kohn, L.J. Sham, *Physical Review* 140 (1965) A1133-A1138.
[42] K. Schwarz, P. Blaha, G.K.H. Madsen, *Computer Physics Communications* 147 (2002) 71-76.
[43] D. Singh, *Planewaves, Pseudopotentials and the LAPW Method*. Kluwer Academic, Boston, MA, 1994.
[44] F. Tran, P. Blaha, *Physical Review Letters* 102 (2009) 226401(4).

[45] J.B. Whalen, D. Ramirez, T. Besara, T. Siegrist, To be published.
[46] V. Johnson, W. Jeitschko, *Journal of Solid State Chemistry* 11 (1974) 161-166.
[47] J. Sun, D. Singh, T. Siegrist, To be published.
[48] C. Kittel, *Introduction to Solid State Physics*. 7th ed.; John Wiley & Sons, Inc., New York, 1996.
[49] N.W. Ashcroft, N.D. Mermin, *Solid State Physics*. Saunders College, Philadelphia, 1976.
[50] F. Wooten, *Optical Properties of Solids*. Academic Press, New York, 1972.